Search for Supersymmetry in opposite-sign same-flavour dilepton events with the CMS detector in proton-proton collisions at $\sqrt{s} = 8$ TeV

vorgelegt von
Jan-Frederik Schulte, M.Sc.
aus Münster

Zusammenfassung

Abstract

Contents

1 Introduction

2 The Standard Model and its extension to Supersymmetry

2.1 The Standard Model of particle physics

2.2 Motivation for extending the Standard Model and Supersymmetry

2.3 Production of lepton pairs in supersymmetric models

2.4 Kinematic edges in the dilepton invariant mass spectrum

3 Experimental setup

3.1 The CERN Large Hadron Collider

The Large Hadron Collider (LHC) [1], located at CERN near Geneva and stretching far into the french countryside, is capable of colliding protons and lead ions at higher energies than any of its predecessors. Also the instantaneous luminosity delivered to the experiments exceeds that of any previous machine at the energy frontier. It was constructed in the tunnel formerly inhabited by the LEP electron-positron collider in $100\,\mathrm{m}$ depths below the surface with a circumference $27\,\mathrm{km}$. It was designed to collide protons at a centre-of-mass energy of $\sqrt{s} = 14\,\mathrm{TeV}$ with instantaneous luminosities of $10^{34}\,\mathrm{s^{-1}m^{-2}}$.

The LHC consists of eight arcs, as shown in Figure 3.1, where superconducting dipole magnets are used to provide a magnetic field of up to $8.3\,\mathrm{T}$ at the highest planned energies to bend the charged particles along the curvature of the tunnel, while quadrupole and other specialised magnets are used to focus the beams. In straight segments between these arcs, LHC infrastructure and the experiments are located. The infrastructure components include the cooling facilities necessary to reach a temperature of $1.9\,\mathrm{K}$ around the ring, the superconducting cavities in which the protons are accelerated by standing electromagnetic waves, collimators for beam cleaning and the beam dump, where the beam is ejected from the LHC at the end of fills. In the other four straight segments the beam is brought into collisions, which are studied by the four large experiments at the LHC. Of these, CMS [2] and ATLAS [3] are multi-purpose detectors with a diverse physics program, while ALICE [3] and LHCb [4] are more narrowly focused on heavy ion collisions and flavour physics, respectively.
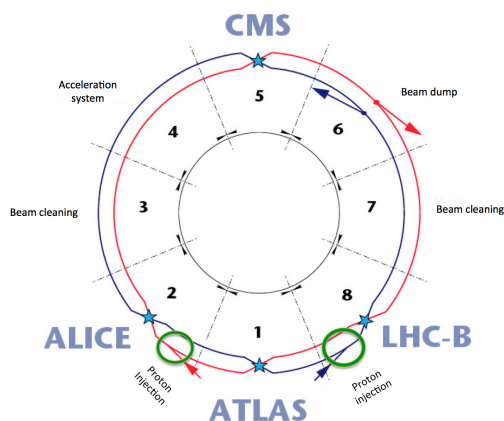
Figure 3.1: Schematic view of the LHC with its eight arcs. The four interaction points, where the experiments are located, are marked with blue stars. Other important parts of the LHC infrastructure are also indicated [5].

The protons circulating the LHC are injected at an energy of $450\,\mathrm{GeV}$ after running trough a chain of pre-accelerators, the Linac2, the Proton Synchrotron Booster (PSB), the Proton Synchrotron (PS) and the Super Proton Synchrotron (SPS). The proton beams are separated into bunches of about 10^{11} particles. Though being $25\,\mathrm{ns}$ by design, corresponding to up to 2808 bunches in the LHC, the smallest spacing between to bunches in time was $50\,\mathrm{ns}$ throughout the running in 2012 and most of 2011. In

these running conditions, after three years of running in the years 2010 to 2012, constituting the so called Run I of the LHC, a centre-of-mass energy of $\sqrt{s} = 8\,\text{TeV}$ has been reached. The instantaneous luminosities delivered to the experiments reached a maximum of $7.7 \cdot 10^{33}\,\text{s}^{-1}\text{m}^{-2}$ in late 2012, as can be seen on the left side of Figure 3.2. The integrated luminosity delivered to the CMS experiments in 2012 was $23.3\,\text{fb}^{-1}$, exceeding that of 2011 by almost a factor of four [6], as shown on the right side of Figure 3.2.
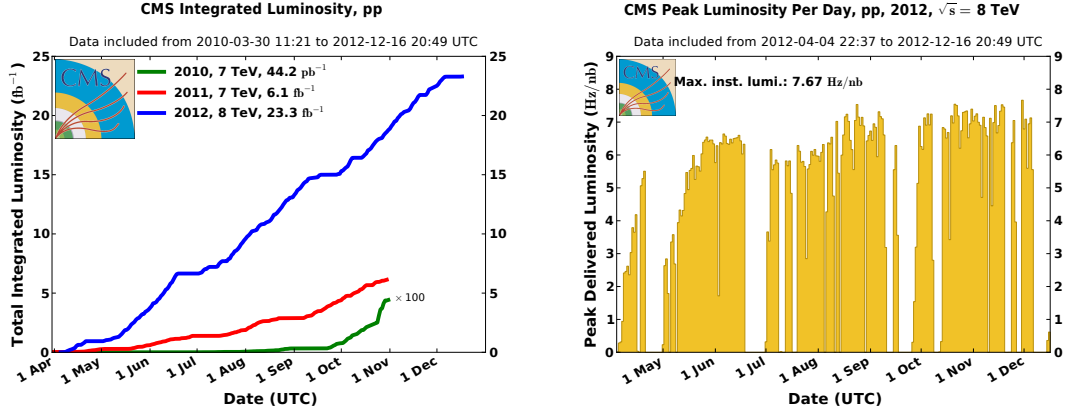

Figure 3.2: Development of instantaneous (left) and integrated (right) luminosity delivered to the CMS experiment. The left plots shows the results for all three years of data taking, while the right one only shows the 2012 data taking.

3.2 The CMS detector

Located in one of the four intersections of the LHC beams, the CMS detector is designed to measure the resulting collisions to high precision. Key ingredients are a high precision measurements of the properties of single particles as well as a good coverage of the 4π solid angle. The central element of the CMS detector is a superconducting solenoid. Cooled to $4.45\,\text{K}$, it is able to produce a homogeneous magnetic field of $3.8\,\text{T}$, which allows to measure the momentum of charged particle by bending their trajectories. As shown in Figure 3.3, the different components of the detector are layered in cylindrical shapes around the interaction point. The magnet encompasses most of the main subdetectors, namely the tracking system which measures the trajectories of charged particles and the electromagnetic and hadron calorimeters, designed to measure the energy of particles. Located outside of the volume of the solenoid are the iron return yoke and muon detectors. This cylindrical structure is complemented on both sides by endcaps, which close the solid angle in the direction of the beams and are partly located outside the volume of the solenoid. The different components are described in more detail in the following.

3.2.1 The tracking system

The trajectory of charged particles can be determined by measuring the signal of the ionization they cause when traversing matter. The tracking system of the CMS detector consists of many layers of silicon pixels and strips. Combining the points at which a charged particle traverses the different layers, the trajectory of this particle can be measured. The bending of this trajectory under the influence of the magnetic field allows to determine the momentum of the particle. The tracking system has a diameter of $2.5\,\text{m}$ and a length of $5.8\,\text{m}$, corresponding to a geometric coverage of $|\eta| < 2.5$. The
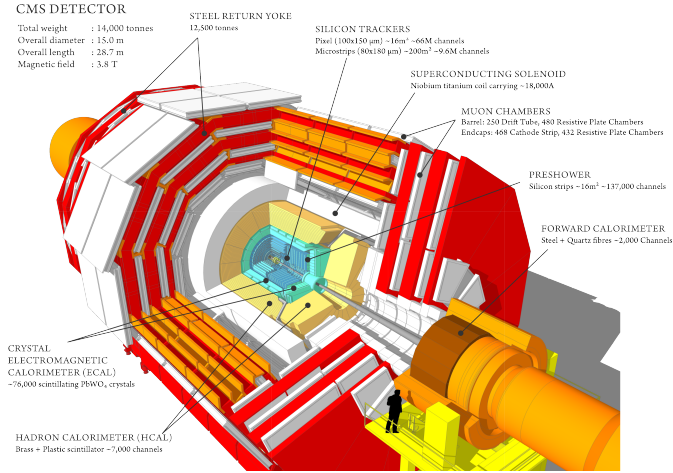
Figure 3.3: Schematic view of the CMS detector [7]. From the inside out, the tracking system is shown in blue, the electromagnetic calorimeter in green, the hadron calorimeter in light yellow, the superconducting solenoid in white, the return yoke in red and the muon system again in white.

tracking detector consists, as shown in Figure 3.4, of the pixel detector (PIXEL) surrounded by various components of the silicon strip tracker.
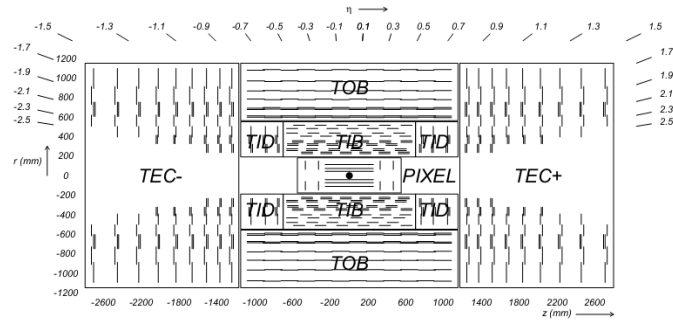

Figure 3.4: Schematic view of the CMS tracking detector. The innermost part shows the pixel detector (PIXEL), surrounded by the tracker inner barrel (TIB) and tracker inner discs (TID). The outermost parts of the tracking detector are the tracker outer barrel (TOB) and the two tracker endcaps (TEC+ and TEC-).

The silicon pixel detector

The innermost part of the tracking system in the pixel detector, which consists of three layers in the barrel region at radii between $4.4\,\mathrm{cm}$ and $10.2\,\mathrm{cm}$, complemented by two discs perpendicular to the beam axis, located at $|z| = 34.5\,\mathrm{cm}$ and $|z| = 46.5\,\mathrm{cm}$. As the particle density is highest close to the interaction point, a high granularity is needed to maintain a low occupancy of the pixel detector. Therefore the pixel detector consists of roughly 66 million pixels with a combined active area of about $1\,\mathrm{m}^2$. Each pixel has a size of $150 \times 100\,\mathrm{\mu m}^2$. The analogue readout of the pixels allows to combine the measurements of neighbouring pixels, bringing the spatial resolution down to 15 to $20\,\mathrm{\mu m}$. This is especially important for the reconstruction of the interaction vertices and the tagging of the secondary vertices from the decay of b-hadrons.

The silicon strip detector

Further away from the interaction point, between $20\,\mathrm{cm}$ and $116\,\mathrm{cm}$, the granularity of the tracking system is reduced. Silicon strip detectors are used, structured in four layers of the tracker inner barrel (TIB), complemented on each side with three discs of the tracker inner discs (TID). All this is surrounded by the six layers of the tracker outer barrel (TOB). The tracker endcaps (TECs) consist of nine discs each. The individual strips have a length of about $10\,\mathrm{cm}$ and a pitch between $80\,\mathrm{\mu m}$ in the two inner layers of the TIB and $183\,\mathrm{\mu m}$ in the four inner layers of the TOB. The single point resolution in TIB and TOB depends on the layout of the specific layer and varies between $23\,\mathrm{\mu m}$ and $53\,\mathrm{\mu m}$.

Stereo modules, constructed by placing two modules back to back, rotated by $100\,\mathrm{mrad}$, are placed in the first two layers of both TIB and TOB, the first two discs of TID and the first two and the fifth discs of the TECs. These allow for 2-D measurements, with a precision of the z position measurement of $230\,\mathrm{\mu m}$ in TIB and $530\,\mathrm{\mu m}$ in TOB.

For high momentum tracks of about $100\,\mathrm{GeV}$ in the region of $|\eta| < 1.6$ a p_T resolution of 1-2% is achieved, while the impact parameter of these tracks can be measured with a resolution of about $10\,\mathrm{\mu m}$.

Compared to other tracking technologies, an all silicon tracking system as used in CMS consists of significantly more material. The material budget lies between 0.4 and 1.8 radiation length X_0, as shown in Figure 3.5. For light charged particles such as electrons this leads to a significant probability to emit bremsstrahlung in while traversing the tracking detector, which has to be taken into account in the reconstruction of particles.
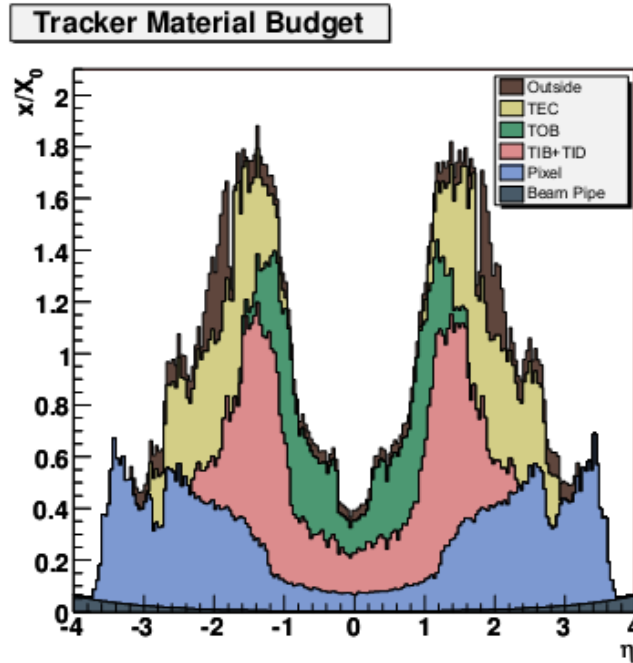

Figure 3.5: Material budget of the CMS tracking detector in units of radiation length X_0 as a function of η.

3.2.2 The electromagnetic calorimeter

The electromagnetic calorimeter (ECAL) measures the energy of electrons and photons. It uses lead tungstate ($PbWO_4$) crystals both as absorber and active material. The electromagnetic shower induced by the electron or photon leads to the emission of scintillation light in the crystal, which is measured at the end of the crystals by avalanche photo diodes (APDs) in the barrel segment of the ECAL and more radiation hard vacuum photo triods (VTPs) in the endcap region. The choice of lead tungstate was driven by the need for a material that is at the same time dense ($8.28\,\mathrm{g/cm^3}$), has a small Molià¨re radius ($2.2\,\mathrm{cm}$) and is fast. About 80% of the scintillation light is emitted after $25\,\mathrm{ns}$, which is the time between two LHC bunch crossing under design conditions. The structure of the ECAL is shown
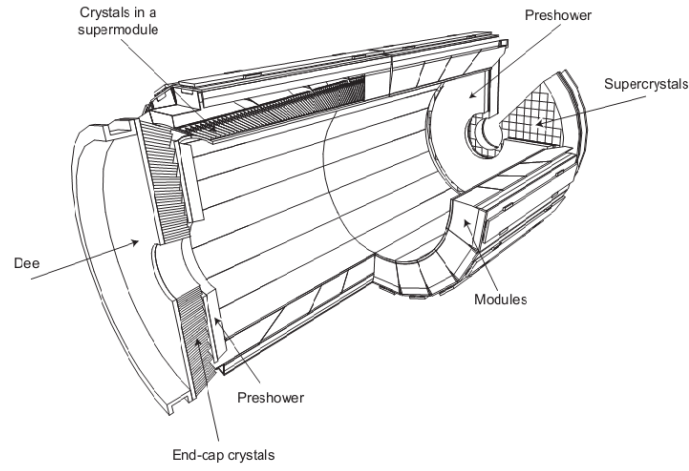

Figure 3.6: Schematic view of the CMS ECAL.

in Figure 3.6. The ECAL barrel (EB) covers the region of $|\eta| < 1.479$ and consists of 61200 crystals. They have a size of $2.2 \times 2.2\,\mathrm{cm^2}$ at the front and $2.6 \times 2.6\,\mathrm{cm^2}$ at the back, with a length of $23\,\mathrm{cm}$, corresponding to 25.8 X_0. In the ECAL endcaps (EE), consisting of 7324 crystal each, they are slightly larger ($2.862 \times 2.862\,\mathrm{cm^2}$ to $3.0 \times 3.0\,\mathrm{cm^2}$) and shorter ($22\,\mathrm{cm}$, corresponding to 24.7 X_0). The EEs extend the geometric coverage of the ECAL to $|\eta| = 3.0$.

In the region of $1.653 < |\eta| < 2.6$ a preshower detector, consisting of two layers of silicon strips and two layers of lead absorber, is installed to distinguish between prompt photons and those from the decay $\pi^0 \to \gamma\gamma$. The strips, oriented perpendicular to each other, have a pitch of $2\,\mathrm{mm}$, allowing to resolve the two showers of the photons from the π^0.

The production of scintillation photons per energy deposit is temperature depend. Therefore the ECAL is kept at a temperature of $18 \pm 0.05\,^\circ\mathrm{C}$, where it is about 4.5 photons per MeV.

The typical resolution of the ECAL is parametrized as

$$\left(\frac{\sigma}{E}\right)^2 = \left(\frac{2.8\%}{\sqrt{E}}\right)^2 + \left(\frac{0.12}{E}\right)^2 + (0.30\%)^2, \qquad (3.1)$$

with three terms describing different sources of uncertainty. The first term includes statistical fluctuation in the production of scintillation light as well as the energy distribution over several crystals. The second term covers such sources of noise as electronic noise or pileup. The constant term accounts for other sources of uncertainties such as calibration errors. The size of the different contributions has been confirmed in test beam measurements [8].

3.2.3 The hadron calorimeter

3.2.4 The muon system

3.3 Data acquisition and event reconstruction

4 Data analysis and event selection

4.1 Trigger and event processing

4.2 Object reconstruction

4.3 Datasets

4.4 Event selection

5 Estimation of Standard Model backgrounds

5.1 Flavour-symmetric backgrounds

5.2 Backgrounds containing a Z boson

5.3 Investigation of possible further backgrounds

5.4 Search for a kinematic edge with a fit

6 Results

6.1 Result of the counting experiment

6.2 Result of the search for a kinematic edge

7 Interpretation in simplified models

7.1 Simplified Models for Supersymmetric Signatures

7.2 The T6bblledge and T6bbslepton model

7.3 Interpretation of the counting experiment in simplified models

8 Outlook to LHC Run II

9 Conclusion

Bibliography

[1] Lyndon Evans and Philip Bryant. LHC Machine. *Journal of Instrumentation*, 3(08):S08001, 2008.

[2] CMS Collaboration. The CMS experiment at the CERN LHC. *Journal of Instrumentation*, 3(08):S08004, 2008.

[3] ATLAS Collaboration. The ATLAS Experiment at the CERN Large Hadron Collider. *Journal of Instrumentation*, 3(08):S08003, 2008.

[4] LHCb Collaboration. The LHCb Detector at the LHC. *Journal of Instrumentation*, 3(08):S08005, 2008.

[5] Particle kickers. https://cds.cern.ch/record/1706606/. Accessed: 2014-08-06.

[6] CMS Collaboration. Public CMS Luminosity Information. https://twiki.cern.ch/twiki/bin/view/CMSPublic/LumiPublicResults?rev=101. Accessed: 2014-08-06.

[7] Cms detector design. http://cms.web.cern.ch/news/cms-detector-design. Accessed: 2014-08-08.

[8] CMS Collaboration. Electromagnetic calorimeter calibration with 7 TeV data. 2010. CMS Physics Analysis Summary EGM-10-003.